PHYSICAL REVIEW B VOLUME 57, NUMBER 10 1 MARCH 1998-II

Angle-resolved photoemission on untwinned $YBa_2Cu_3O_{6.95}$. I. Electronic structure and dispersion relations of surface and bulk bands

Matthias C. Schabel
Department of Applied Physics, Stanford University, Stanford, California 94305

C.-H. Park
Department of Applied Physics, Department of Physics, and Stanford Synchrotron Radiation Laboratory, Stanford University, Stanford, California 94305

A. Matsuura
Department of Applied Physics and Department of Physics, Stanford University, Stanford, California 94305

Z.-X. Shen
Department of Applied Physics and Stanford Synchrotron Radiation Laboratory, Stanford University, Stanford, California 94305

D. A. Bonn, Ruixing Liang, and W. N. Hardy
Department of Physics and Astronomy, University of British Columbia, Vancouver, British Columbia, Canada V6T 1Z1

(Received 28 July 1997)

Angle-resolved photoemission studies of the dispersion relations and polarization dependence of bands in the near E_F region of untwinned $YBa_2Cu_3O_{7-\delta}$ (Y123) single crystals reveal previously unseen details of the electronic structure and significantly expand our understanding of this system. We find that the narrow, intense feature seen along ΓY in Y123 and $YBa_2Cu_4O_8$ (Y124) is best explained as a surface termination effect related to the quasi-one-dimensional CuO_3 chains, masking underlying electronic states at the Fermi energy. Many of the previously puzzling photoemission results from these materials are readily understood within this context, including the failure to observe a superconducting gap, the weak effect of deoxygenation on the photoemission spectra for $\delta \leq 0.5$, the weak dependence of this feature on Pr doping, and the strong photon energy dependence of the photoemission spectra. Our data, taken in the superconducting state, reveal the bilayer splitting and c-axis dispersion of the CuO_2 plane bands. We also find evidence for a one-dimensional chain Fermi surface parallel to the ΓX direction, but see no indication of the BaO derived ‘‘stick’’ pocket centered on the S point. [S0163-1829(98)04910-8]

I. INTRODUCTION

Observation of a highly anisotropic superconducting gap in angle-resolved photoelectron spectroscopy (ARPES) measurements on $Bi_2Sr_2CaCu_2O_{8+\delta}$ (Bi2212) is a major piece of evidence supporting the d-wave pairing hypothesis for high-T_c materials.[1] The clear onset of superconductivity and modification of the spectral weight at T_c sparked a proliferation of studies of the electronic structure of this material in various temperature and doping regimes. These have repeatedly provided new insight into the cuprates and have been a fertile source of grist for theorist’s mills. One of the persistent puzzles in the ARPES community was the inability to reproducibly observe, until recently,[2] a similar gap in Y123 despite intense efforts and demonstrably superior sample quality.[3] This directly contradicts a large body of evidence from other techniques, including Josephson tunneling,[4] microwave absorption,[5] and scanning superconducting quantum interference device microscopy,[6] which clearly reveal the appearance of a superconducting gap of comparable magnitude and anisotropy to that seen in Bi2212.[7] The absence of a gap is also inconsistent with scanning tunneling microscopy (STM) studies,[8] which are even more surface sensitive than ARPES. It is also of great importance to establish a body of reliable ARPES data on another class of the cuprates in order to differentiate those features which are peculiar to the Bi-based compounds but not critical for the superconducting properties from those which are universal to the cuprates and are, therefore, relevant underlying aspects of their electronic structure.

The primary structural distinction between materials in the Y123/Y124 family and other cuprate superconductors is the presence of uniaxially aligned CuO_3 chains in the charge reservoir layers. In the case of Y123 there is one chain per unit cell, while Y124 has two staggered chains; from the point of view of band theory the main difference between these two is that the chains mediate electron transport along the c axis in Y123, leading to strong dispersion in this direction, while the chain geometry in Y124 frustrates conduction, with consequent suppression of dispersion.[9–11] Nevertheless, band calculations predict splitting of the bonding and antibonding bilayer orbitals of comparable magnitude for both compounds. Generally, the lack of a gap in Y123 has been attributed to surface effects such as reconstruction or oxygen loss, which could lead to a surface not representative of the bulk. However, photoemission, low-energy electron diffraction, and STM all provide evidence that the surface is well ordered when cleaved and maintained at low tempera-

0163-1829/98/57(10)/6090(17)/$15.00

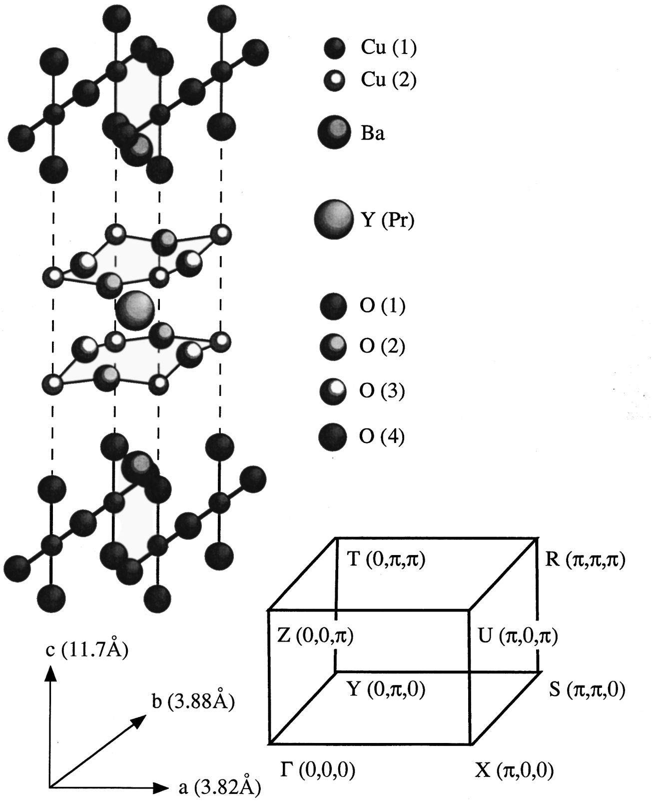

FIG. 1. The crystal structure of Y123, showing the planar CuO_2 bilayers separated by Y atoms and the linear CuO_3 chains running parallel to the b axis. One octant of the Brillouin zone is shown in the same orientation, with the standard notation for the high-symmetry points.

ture, with a mixed termination due to the lack of an inversion symmetric cleavage plane. Furthermore, low-energy valence-band peaks, qualitatively similar to those seen in Bi2212, are clearly observed in ARPES studies of these materials. In the context of this paper we refer to the dispersive features seen in angle-resolved photoemission as quasiparticles for convenience. This usage is not intended, explicitly or implicitly, to give credence to any particular theoretical interpretation. We have undertaken an extensive investigation of untwinned crystals of the highest quality in order to elucidate the important aspects of the Y123 electronic structure and explain the observed variance between ARPES data on Y123 and Bi2212.

Of the many photoemission studies performed on Y123,[12] including extensive work on oxygen doping,[13,14] all but two used twinned crystals in which the quasi-one-dimensional (1D) CuO_3 chains are randomly oriented in domains rotated 90° relative to each other, while the two untwinned studies[15,14] did not fully exploit the photon polarization dependence. Twinning mixes the normally inequivalent $\Gamma XS\Gamma$ and $\Gamma YS\Gamma$ octants of the Brillouin zone (BZ), which are quite anisotropic in local-density approximation (LDA) calculations of the band structure and Fermi surface, including regions of $\mathbf{k}$ space where the superconducting gap is expected to be largest. The crystal structure and BZ notation for untwinned Y123 are shown in Fig. 1; twinned crystals have domains rotated 90° with respect to each other.

One of the most intriguing features of the electronic structure of Y123 is the extremely narrow and intense peak lying approximately 10 meV below the Fermi energy which is seen near the X and Y points in twinned samples. This peak appears to be essentially nondispersive parallel to the $\Gamma X/\Gamma Y$ direction and strongly dispersive along XS/YS, forming what has been referred to as an extended van Hove singularity (evHs). It also manifests unusually strong photon energy dependence, being seen most strongly at $h\nu = 17$ and 28 eV, and also at 50 and 74 eV.[16] In their early study of an untwinned single crystal of Y123, Tobin *et al.*,[15] observed this feature only near the Y point, and concluded that it was correlated with the CuO_3 chains. A similar conclusion was drawn for Y124 crystals by Campuzano[17] *et al.*, based on the relationship between X/Y asymmetry and the uniformity of the cleaved sample surface, and for Y123 based on the results of oxygen doping dependence.[16] However, observation of the peak along ΓY placed the nondispersive direction parallel to the chain axis, rather than perpendicular as would be expected for quasi-1D states. This counterintuitive result is also inconsistent with both LDA predictions of a chain-derived Fermi sheet parallel to the ΓX axis and the chain Fermi surface determined from positron annihilation studies of untwinned crystals.[18] Subsequent photoemission work interpreted the evHs as a CuO_2 plane-derived feature arising from the chain-induced orthorhombic distortion, and implicated the resulting density of states singularity as a possible origin for the high transition temperature.[19–21] Much of this work was driven by the observation of an extended flat band near the Fermi energy in ARPES studies of Bi2212, even though that feature derives from a much broader band in the normal state and exhibits clear and dramatic modification in line shape on passing into the superconducting state.

We believe that the later studies endorsing the evHs interpretation of the feature at the Y point in Y123 have not paid sufficient attention to the highly one-dimensional character of this feature and other aspects of the data. Our results, obtained on untwinned Y123 crystals of exceptional quality, lead us to a different picture of the electronic structure in Y123 and Y124 more consistent with earlier work on twinned crystals, and reveal numerous previously unobserved features. These data indicate that the near-E_F electronic structure along the b axis is strongly masked by the presence of a narrow and intense surface resonance arising primarily from the quasi-1D CuO_3 chains, making untwinned single crystals essential to have any hope of resolving a gap. In addition, we find that varying the sample orientation with respect to the photon polarization is crucial for a complete understanding of the electronic structure of Y123, and we observe polarization effects which are not readily explicable in terms of simple matrix element arguments.

II. EXPERIMENTAL TECHNIQUE

Much of the experimental methodology for photoemission studies of Y123 has been discussed in a thorough review by Veal and Gu.[3] In this paper we focus primarily on the low-binding energy region within 1 eV of E_F; details of the valence-band electronic structure, including the peak appearing at 1 eV binding energy, do not appear to have the same strong dependence on the a/b-axis asymmetry.[15] Our data on

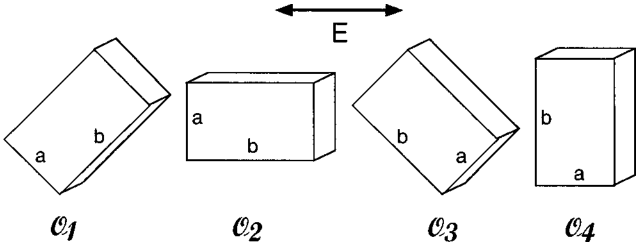

FIG. 2. The four distinct sample orientations possible in our experimental geometry. Plane polarized synchrotron radiation is at an angle of 45° off normal, with the component of **E** parallel to the sample surface as indicated and an additional component parallel to the c axis. Chains are aligned along the b axis, indicated by the long axis of the crystal in the figure. The inequivalence of $\mathcal{O}_1$ and $\mathcal{O}_3$ arises from symmetry breaking in our spectrometer geometry.

this feature is briefly discussed in Sec. IV. Orientation of the fourfold axis of samples is performed *ex situ* by Laue diffraction. Due to growth asymmetry, the chain axis may be determined visually as the long axis of the crystal; the accuracy of visual orientation was verified with x-ray diffraction. All studies were performed on crystals of extremely high quality (typical transition widths of 0.25 K), cleaved and maintained at a constant temperature of 20 K to avoid the surface degradation which is seen with both photoemission and STM for temperatures above ≈ 40 K.[22,8] Photoemission experiments were performed in UHV at the Stanford Synchrotron Radiation Laboratory (SSRL) undulator beamline 5-3, with a chamber base pressure less than 5×10^{-11} torr. Spectra were acquired at an energy resolution of 50 meV, with an angular acceptance of $\pm 1°$; higher resolution would have compromised the overall counting rate and would have made it impossible to perform such an extensive mapping on a single sample.

In our experimental geometry there are three possible distinct orientations $\mathcal{O}_1$, $\mathcal{O}_2$, and $\mathcal{O}_4$, of our samples with respect to linear photon polarization, shown in Fig. 2. A fourth orientation $\mathcal{O}_3$, with the plane component of **E** parallel to ΓS, is nearly equivalent to $\mathcal{O}_1$ with the exception that the momentum component of the outgoing photoelectron relative to the photon momentum is different due to the off-normal photon incidence and the details of our ARPES system. Spectra were taken over the entire Brillouin zone (BZ) in two of these orientations, $\mathcal{O}_1$ and $\mathcal{O}_2$, and along the high-symmetry directions ΓX, ΓY, ΓS, XS, and YS in $\mathcal{O}_3$ and $\mathcal{O}_4$ on one sample and along various symmetry directions on numerous other crystals to verify the consistency of our results for different samples and cleaves. In the figures, all spectra are normalized to the integrated weight well above the Fermi level. This spectral weight, structureless in **k** space, arises from inelastically scattered valence electrons excited by higher-order photons passing through the synchrotron monochromator.

III. SURFACE TERMINATION

As mentioned in the Introduction, the low-temperature STM studies of Edwards *et al.*,[8,23] clearly resolve regions of chains interspersed with indistinct stepped regions whose height is consistent with that expected for BaO planes. These results provide strong evidence for a mixed CuO_3/BaO surface termination in cleaved Y123 crystals. Photoemission corroborates this, revealing a strong Ba $5p$ surface shifted component, shown in Fig. 3, which is indicative of inequivalent bulk and surface Ba coordinations as would arise from a near surface BaO layer.[24] Resolving a similar shift in the chain Cu(1) levels is unfortunately complicated by the presence of two structurally inequivalent Cu atoms in the bulk unit cell, in addition to two possible inequivalent surface sites and the presence of satellite structures in the Cu core levels.

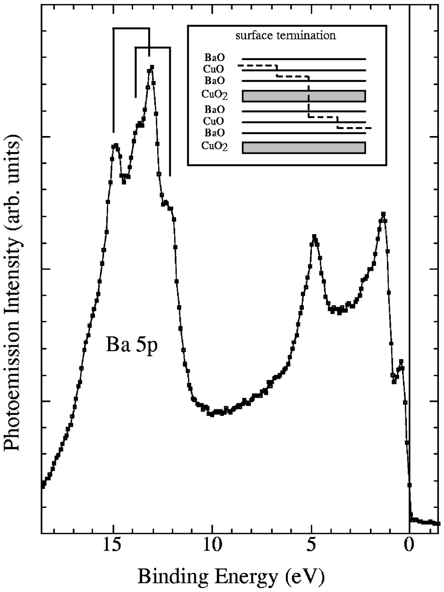

FIG. 3. The full valence band of YBCO, showing distinct bulk and surface shifted Ba $5p$ core levels. While there can be substantial sample to sample variation in the precise magnitude of the surface core-level shift, it can be clearly seen in nearly all spectra, indicating the presence of significant regions of BaO surface termination. The inset shows a schematic of the surface termination of cleaved Y123, with stepped terraces of BaO and CuO_3 chains, based on our data and low-temperature STM results.

It is well known from studies of the electron attenuation length in photoemission experiments that the mean free path of unscattered photoelectrons at the photon energies used in ARPES experiments is extremely short, on the order of 5 Å.[25] This fact, and the relatively large c-axis lattice constant of Y123 (11.7 Å), combine to make the surface contribution in our spectra a substantial fraction of the total signal. A simple layer model allows us to quantitatively estimate the contribution of the surface and subsurface Ba atoms to the total photoemission intensity. We assume a mixed termination of BaO and CuO_3 with equal areas for both terminations, shown schematically in the inset of Fig. 3, make the approximation that the various atomic planes are equally spaced by a distance of $d=c/6$, and regard all subsurface Ba atoms as equivalent to those in the bulk material. In this case, the Ba surface component comes entirely from the BaO surface, and the relative intensities can be expressed as

$$I_{\rm Ba}^{\rm surf}=\left(\frac{1}{I_{\rm Ba}^{\rm total}}\right), \tag{1}$$

$$I_{\mathrm{Ba}}^{\mathrm{bulk}}=\left(\frac{1}{I_{\mathrm{Ba}}^{\mathrm{total}}}\right)(e^{-d/\lambda}+e^{-5d/\lambda}+e^{-4d/\lambda}+e^{-6d/\lambda})\sum_{n=0}^{\infty}e^{-nc/\lambda}, \tag{2}$$

$$I_{\mathrm{Ba}}^{\mathrm{total}}=1+(e^{-d/\lambda}+e^{-5d/\lambda}+e^{-4d/\lambda}+e^{-6d/\lambda})\sum_{n=0}^{\infty}e^{-nc/\lambda}. \tag{3}$$

Noting that the sum may be expressed in closed form as

$$\sum_{n=0}^{\infty}e^{-nc/\lambda}=\frac{e^{c/\lambda}}{e^{c/\lambda}-1}, \tag{4}$$

we can evaluate the relative contributions using 11.7 Å for c and 5 Å for λ. This gives us a surface to bulk ratio for the Ba core levels of 82%, in good qualitative agreement with the nearly equal contributions of the surface (high binding energy) and subsurface (low binding energy) features seen in Fig. 3, as well as with the results of studies of the Ba $4d$ core levels reported by Veal *et al.*[3] We can also establish that the electron escape depth estimate of 5 Å is a comparatively good one by calculating the surface to bulk ratio for $\lambda=10$ Å, which gives a value of 35%—significantly smaller than observed.

A similar analysis may be performed for the Cu valence-state intensities, allowing estimation of the contribution of ''bulk'' (subsurface) chain states relative to the surface chain states and bulk plane states. On the general grounds discussed above, we expect the surface contribution to the chain states to dominate the bulk chain emission. Assuming that the intrinsic emission from all states is equal (i.e., ignoring matrix element effects), and modifying the model used above for the Cu states gives

$$I_{\mathrm{chain}}^{\mathrm{surf}}=\left(\frac{1}{I_{\mathrm{Cu}}^{\mathrm{total}}}\right), \tag{5}$$

$$I_{\mathrm{plane}}^{\mathrm{bulk}}=\left(\frac{1}{I_{\mathrm{Cu}}^{\mathrm{total}}}\right)(e^{-2d/\lambda}+e^{-4d/\lambda}+e^{-d/\lambda}+e^{-3d/\lambda})\sum_{n=0}^{\infty}e^{-nc/\lambda}, \tag{6}$$

$$I_{\mathrm{chain}}^{\mathrm{bulk}}=\left(\frac{1}{I_{\mathrm{Cu}}^{\mathrm{total}}}\right)(e^{-6d/\lambda}+e^{-5d/\lambda})\sum_{n=0}^{\infty}e^{-nc/\lambda}, \tag{7}$$

$$\begin{aligned}I_{\mathrm{Cu}}^{\mathrm{total}}=1+(&e^{-6d/\lambda}+e^{-5d/\lambda}+e^{-2d/\lambda}+e^{-4d/\lambda}+e^{-d/\lambda}\\&+e^{-3d/\lambda})\sum_{n=0}^{\infty}e^{-nc/\lambda}.\end{aligned} \tag{8}$$

Evaluating the sums for the above values of c and λ leads to contributions of 59, 32, and 9% for the bulk planes, surface chains, and bulk chains, respectively. Even allowing for an escape depth twice as large (i.e., 10 Å) only changes the relative contributions of plane, surface, and chain to 64, 18, and 18%. Based on these estimates, it is likely that the bulk chain features of the electronic structure will only make a small contribution to the overall photoemission spectra unless there are significant matrix element differentials for photoemission from one subsystem or the other.

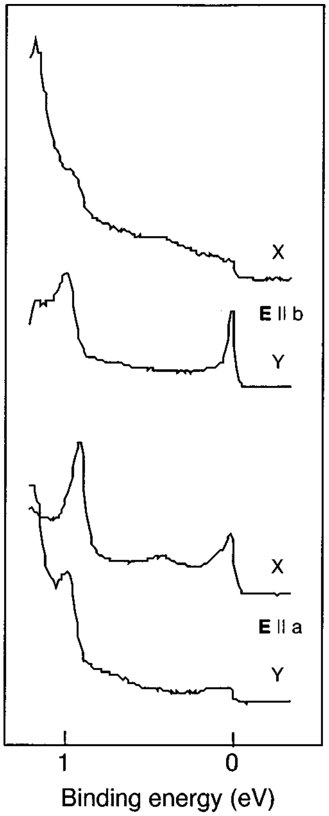

FIG. 4. ARPES spectra from the X and Y points for photon polarization parallel to b, the chain axis (upper curves) and parallel to a (lower curves). The 1 eV peak is seen most clearly at X for emission parallel to photon polarization, and most weakly for perpendicular emission, consistent with an initial state having $d_{x^2-y^2}$ symmetry. Contrasting with this, the peak at Y appears in both polarizations, with some weaker enhancement for parallel emission. The binding energy also differs between the two points in $\mathbf{k}$ space, being 0.92 eV at X and 0.98 eV at Y.

IV. THE 1 eV PEAK

A rather pronounced feature of the valence-band electronic structure of Y123 and Y124 is the narrow feature found near $X(Y)$ at a binding energy of approximately 1 eV. Olson *et al.*, argue that this feature is actually a robust aspect of the electronic structure of all cuprate superconductors,[26] while others have contended that it arises from surface termination effects extrinsic to the bulk.[27,28] The emphasis of the present paper is on the low-lying excitations in untwinned Y123, but a brief discussion of the polarization dependence of the 1 eV peak in these samples is presented here for completeness. Figure 4 shows data at X and Y for photon polarizations parallel to the inequivalent cubic axes. In the upper part, for $\mathbf{E}\|b$, we can clearly observe the feature at Y, while it is almost completely absent at X. The lower part, for $\mathbf{E}\|a$, shows a dramatic increase in the intensity at X, while Y is somewhat attenuated, but less strongly than at X. This behavior at X is consistent with an initial state having p_z, d_{z^2}, or $d_{x^2-y^2}$ symmetry, while the feature at Y appears to be formed from an admixture of states having other symmetries. A recent paper by Pothuizen *et al.* interprets this feature as a nonbonding state of the cuprate planes in these materials.[29] We observe a clear difference in both the binding energies and line shapes of the two peaks, with the state lying at 0.92

TABLE I. Selection rules for initial states having varying symmetries corresponding to the sample geometries shown in Fig. 2. In the table, e indicates even symmetry with respect to the plane of electron emission, and *o* indicates odd symmetry. A ''yes'' denotes an allowed transition and ''no'' a disallowed one.

Orientation	$\langle i\vert$	$\mathbf{A}\cdot\mathbf{P}$	$\vert f\rangle$	Allowed
$\mathcal{O}_1/\mathcal{O}_3$				
	o ($d_{x^2-y^2}$)	o	e ($\mathbf{k}\perp\mathbf{E}$)	Yes
	o ($d_{x^2-y^2}$)	e	e ($\mathbf{k}\Vert\mathbf{E}$)	No
	e (d_{xy})	o	e ($\mathbf{k}\perp\mathbf{E}$)	No
	e (d_{xy})	e	e ($\mathbf{k}\Vert\mathbf{E}$)	Yes
	e (p_z/d_{z^2})	o	e ($\mathbf{k}\perp\mathbf{E}$)	No
	e (p_z/d_{z^2})	e	e ($\mathbf{k}\Vert\mathbf{E}$)	Yes
$\mathcal{O}_2/\mathcal{O}_4$				
	e ($d_{x^2-y^2}$)	o	e ($\mathbf{k}\perp\mathbf{E}$)	No
	e ($d_{x^2-y^2}$)	e	e ($\mathbf{k}\Vert\mathbf{E}$)	Yes
	o (d_{xy})	o	e ($\mathbf{k}\perp\mathbf{E}$)	Yes
	o (d_{xy})	e	e ($\mathbf{k}\Vert\mathbf{E}$)	No
	e (p_z/d_{z^2})	o	e ($\mathbf{k}\perp\mathbf{E}$)	No
	e (p_z/d_{z^2})	e	e ($\mathbf{k}\Vert\mathbf{E}$)	Yes

eV at X and at 0.98 eV at Y, indicative of significant chain-induced anisotropy. Our observations also clarify the appearance of multiple features in the twinned data as being a consequence of crystalline anisotropy rather than constituting two distinct states.

V. ELECTRONIC STRUCTURE

Fragmentary band dispersions along high-symmetry directions in the Brillouin zone have been presented in previous studies, but these have been tainted by the mixing of inequivalent octants of the zone from twinning. Here we present a complete set of data for the high-symmetry directions ΓS, ΓX, ΓY, XS, and YS, taken on a single untwinned sample with a photon energy of 28 eV in each of the sample geometries shown in Fig. 2, along with a partial data set taken at 21 eV. The consistency of our ARPES results has been verified on numerous other samples. In each set of energy distribution curves the identifiable quasiparticle peaks are marked with an open circle. Despite the intrinsic breadth of these features (comparable to the dispersive plane bands seen in photoemission data on Bi2212), our statistics are sufficiently good to allow accurate identification of the centroid in most cases. In Table I, selection rules based on free-electron final states are tabulated for various initial-state symmetries and sample geometries, allowing approximate attribution of various bands based on their behavior with respect to polarization orientation.

Figure 5 shows energy distribution curves (EDC's) along the ΓS high-symmetry direction, with the upper panels showing dispersions for $h\nu=28$ eV and the lower ones for $h\nu=21$ eV. For orientations $\mathcal{O}_1$ and $\mathcal{O}_3$, in which the cubic axes are rotated 45° with respect to incident photon polarization, there are two symmetry inequivalent directions for electron emission along ΓS, corresponding to initial states with $\mathbf{k}\Vert\mathbf{E}$ and $\mathbf{k}\perp\mathbf{E}$. In Y123 the presence of the one-dimensional chains breaks the tetragonal symmetry. Nevertheless, the resulting orthorhombic structural distortion of the plane sheets is a small one. For this reason, we discuss state symmetries within the context of approximately tetragonal behavior, although some unusual matrix element effects discussed below may stem from the orthorhombicity. From the selection rules (Table I), we see that emission from initial states with $d_{x^2-y^2}$ symmetry is enhanced for $\mathbf{k}\perp\mathbf{E}$ and emission from states having d_{xy}, p_z, or d_{z^2} symmetry is enhanced for $\mathbf{k}\Vert\mathbf{E}$. Panel 5(a), corresponding to the former, clearly reveals two distinct quasiparticle excitations having binding energies at Γ of 0.53 and 0.22 eV, respectively. These features both exhibit upward dispersion, with the lower binding energy peak appearing to cross the Fermi surface at around 25% of the ΓS distance, and the higher binding energy near 35%. In contrast panel 5(b), for which $\mathbf{k}\Vert\mathbf{E}$, reveals two peaks at the expected energies at Γ but, while spectral weight can be seen to shift and diminish near the crossing points, the quasiparticle features are significantly less distinct and attribution of a peak centroid is difficult. This indicates that the observed states are predominantly derived from the Cu $3d_{x^2-y^2}$ orbitals, with weak admixture of states of different symmetry. Panel 5(c), in which the sample crystal is rotated 90° with respect to $\mathcal{O}_1$, shows some unusual features which cannot be explained using the two-dimensional selection rules. While the two features remain apparent at Γ, the dispersion of the high binding energy peak becomes difficult to discern, and it and the lower energy state appear to overlap strongly as they approach the Fermi-surface crossing. Panel 5(d), on the other hand, shows the EDC's for emission parallel to the polarization for which we expect suppression of the $3d_{x^2-y^2}$ states. Surprisingly, in these spectra the dispersion of the higher energy quasiparticle remains clearly discernible, if somewhat weaker, while the low-energy state is difficult to discriminate. This unusual behavior may stem from hybridization of plane and chain states combined with the symmetry breaking of the off-normal photon incidence. Also, since data were taken in $\mathcal{O}_3$ last, there may be some aging effects, although no dramatic

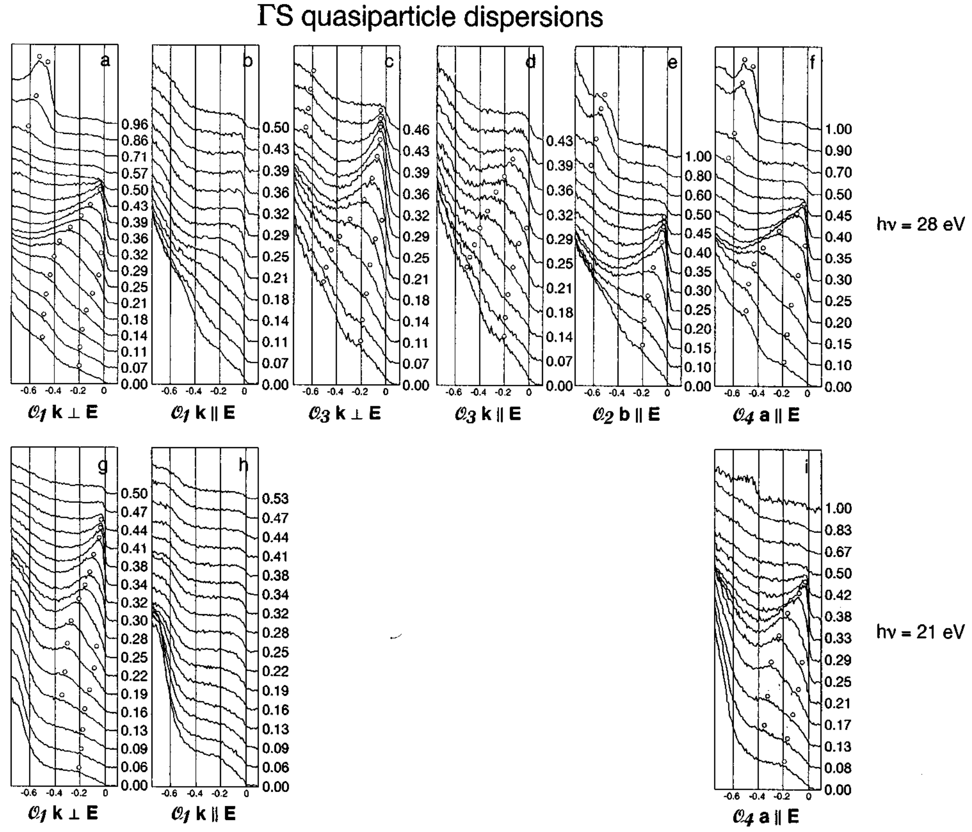

FIG. 5. Energy distribution curves along the ΓS symmetry line. Identifiable quasiparticle peaks are indicated by open circles, with the **k** value of each EDC given as a fraction of the total distance between high-symmetry points.

qualitative changes in spectra were noticed over the course of the experiment.

EDC's along ΓS for sample orientations $\mathcal{O}_2$, with $b \| \mathbf{E}$, and $\mathcal{O}_4$, with $b \perp \mathbf{E}$, are shown in panels 5(e) and 5(f), respectively. Again, the relevant selection rules for the low-lying states are given in Table I. However, in these geometries an additional effect must be considered where the states derived from CuO_3 chains are concerned. To the extent that we may consider these chains to be ideally one-dimensional and uncoupled to each other and to the planes, it is clear that photon polarization perpendicular to the chains will always lead to suppression of emission from chain states as there is no mechanism for excitation of quasiparticles. Therefore, the chain states which are mainly comprised of Cu(1) $3d_{x^2-y^2}$-O(1) $2p_y$ hybrids, will only be observed in orientations having a chain component of the polarization ($\mathcal{O}_1$, $\mathcal{O}_2$, and $\mathcal{O}_3$) and will be absent in $\mathcal{O}_4$ for which $b \perp \mathbf{E}$. Panel 5(e), with polarization parallel to the chain axis, shows behavior reminiscent of that in panel 5(c), with the low binding energy quasiparticle being more prominent at Γ, gradually overlapping with weight from higher energies as the Fermi-surface crossing is approached. Panel 5(f), from $\mathcal{O}_4$ for which chain emission should be strongly suppressed, quite clearly shows both the low and high binding energy features, each being comparatively easily tracked dispersing in **k** to the Fermi surface. This behavior, contrasted with that seen in panel 5(e), strongly supports the attribution of these two bands to CuO_2 plane-derived states, while the enhancement of the low binding energy peak in $\mathcal{O}_2$ suggests significant chain-plane band overlap or hybridization. Our measured bandwidth for the high-energy feature is 0.52 eV, somewhat larger than the 0.35 eV width observed in the related insulating cuprate $\mathrm{Sr_2CuO_2Cl_2}$,[30] but still significantly renormalized from the 0.75 eV predicted by density-functional calculations. The observed diminishment of the correlation-induced bandwidth narrowing is likely a consequence of weakening of antiferromagnetic fluctuations in the metallic optimally doped compound relative to the insulator. However, it should be noted that the photoemission feature from this doped compound is still very broad, unlike the expected behavior of a Fermi-liquid quasiparticle. This breadth is likely a hallmark of strong correlation effects in these materials.

Turning to an excitation energy of $h\nu = 21$ eV, in $\mathcal{O}_1$, we again see two clear and dispersive quasiparticle features for $\mathbf{k} \perp \mathbf{E}$ [panel 5(g)], which are essentially completely suppressed for $\mathbf{k} \| \mathbf{E}$ [panel 5(h)], consistent with a large degree of Cu $3d_{x^2-y^2}$ parentage. Panel 5(i), for photon polarization perpendicular to the chains, reveals essentially identical behavior, with both the low and high binding energy components clearly resolved. Significant enhancement of a higher-energy feature found near 0.75 eV at this photon energy makes resolution of the high-energy state near Γ difficult, but it becomes clearly discernible by 13% of ΓS.

An overall picture of the dispersions along ΓS is shown in Fig. 6, with the energies of quasiparticle features identified in the various panels of Fig. 5 plotted against normalized fraction of the ΓS distance. There are several key observations to be made from the figure. First, the two clearly resolved quasiparticle features of plane origin are most sensibly attributed

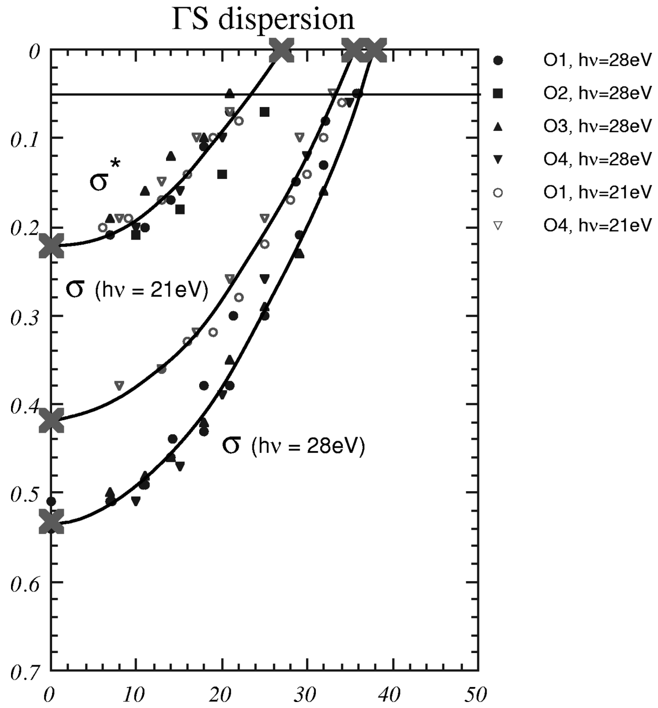

FIG. 6. Energy dispersion of quasiparticles along the ΓS symmetry line. Solid symbols indicated data points taken for $h\nu=28$ eV, while open symbols are for $h\nu=21$ eV. Band minima are indicated by crosses along the vertical axis, while the corresponding Fermi-surface crossings are marked with crosses on the horizontal axis. The thick solid lines are smooth interpolations through the data as guides to the eye, while the thin horizontal line indicates the instrument resolution.

to the bonding and antibonding plane states of the CuO_2 bilayers. The lower binding energy feature (the antibonding $\sigma^\star$ state) dispersing from 0.22 eV at Γ to a crossing at near 25% of ΓS shows essentially no dispersion in k_z, with the data points from $h\nu=21$ and 28 eV lying on the same curve. In contrast, the higher energy feature (bonding σ state) found at 0.53 eV at Γ for $h\nu=28$ eV and crossing the Fermi surface around 35% of ΓS, reveals significantly different dispersion at $h\nu=21$ eV, with the maximum binding energy at Γ decreasing to approximately 0.42 eV, but with a nearly identical Fermi-surface crossing position. By taking data along identical lines in (k_x,k_y) at different photon energies we sample different values of k_z. Thus, the observed energy dispersion of the plane bonding band with $h\nu$ is most simply interpreted as a hallmark of c axis (k_z) dispersion of this state. Also significant is the degeneracy of the Fermi-surface crossings for the two photon energies, implying that the c-axis dispersion which is large at high binding energies becomes vanishingly small at the Fermi energy. This result is consistent with LDA calculations which predict bilayer splitting of the bonding and antibonding plane states in Y123, although our observed magnitude of 0.2 to 0.3 eV (depending on k_z) is approximately one half the value expected from the *ab initio* results.

EDC's corresponding to cuts along the ΓX line are shown in Fig. 7. The orthorhombicity of the crystals induced by the presence of the chains makes the X and Y points inequivalent, so the simple symmetry analysis applied to states along ΓS above is not adequate to unravel the character of the states along ΓX and ΓY. Again, as for the ΓS cuts, we see unusual differences in the spectra taken in $\mathcal{O}_1$ and $\mathcal{O}_3$, shown for $h\nu=28$ eV in panels 7(a) and 7(c). Panel 7(a) clearly shows a gradual upward dispersion and decreased width of both the higher and lower energy quasiparticles at Γ, along with the appearance of a weakly dispersive third feature as a shoulder slightly below the peak near E_F at X. In a similar manner, the two quasiparticles at Γ in panel 7(c) disperse upward, although only the lower energy feature sharpens measurably. In addition, the shoulder feature is not present, within the experimental resolution, in this set of data. Turning to the data from $\mathcal{O}_2$ and $\mathcal{O}_4$, we first note that, following the selection rules in Table I, emission from states of $d_{x^2-y^2}$ symmetry is forbidden along ΓX in the former and allowed in the latter. Also, again assuming one-dimensionality of the chains, emission from chain states should be strongly suppressed in the latter geometry as the photon polarization is perpendicular to the chains and must, therefore, couple weakly. Examination of panel 7(d) confirms this; while the features are qualitatively similar to those seen in panel 7(a), their intensities relative to the incoherent background are significantly diminished. Panel 7(e), for which plane state emission should be maximized and chain emission minimized,

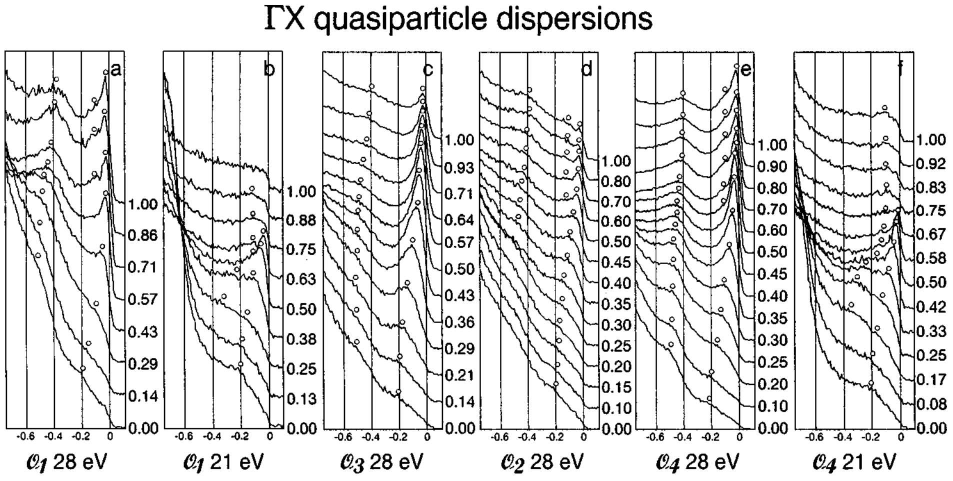

FIG. 7. Energy distribution curves along the ΓX symmetry line, plotted as in Fig. 5.

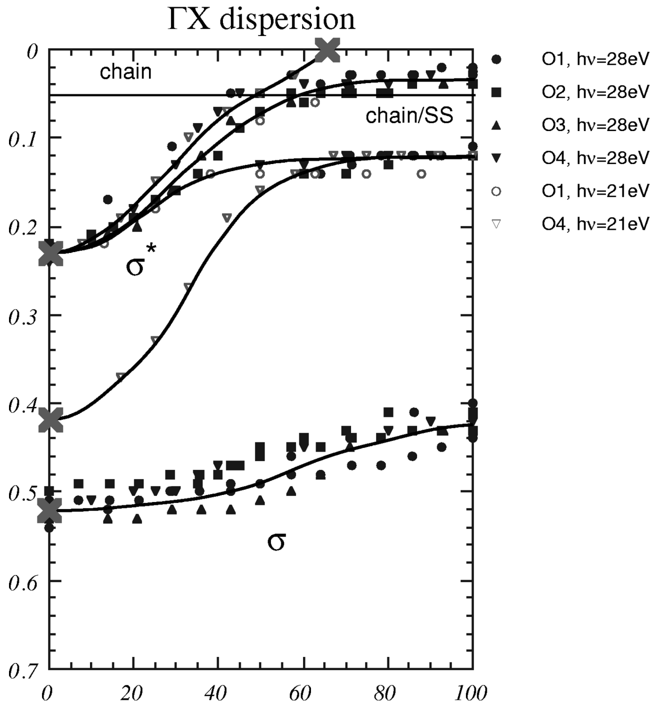

FIG. 8. Energy dispersion of quasiparticles along the ΓX symmetry line, plotted as in Fig. 6.

also reveals three quasiparticle features, the high and low binding energy structures being relatively strong, and the shoulder feature being comparable in relative intensity to that of panel 7(a).

At a photon energy of $h\nu=21$ eV, we observe some interesting changes in the spectra. Panel 7(b) ($\mathcal{O}_1$) shows the feature at 0.22 eV disperse upward toward X, but, unlike the 28 eV data, it continues upward through the Fermi surface, crossing near 60% of ΓX. Also different from the 28 eV data is the clear upward dispersion of the higher energy quasiparticle, which moves to lower binding energy, forming an extended saddle-point singularity with a binding energy of 0.13 eV at X presumably corresponding to the shoulder seen at $h\nu=28$ eV. Data for $\mathcal{O}_4$ is presented in panel 7(f). The low binding energy feature behaves in an essentially identical manner to that in panel 7(b), dispersing toward the Fermi level, then showing a clear crossing round 60% of ΓX. Similarly, the high binding energy feature appears to disperse toward E_F, then flatten out as the shoulder at 0.13 eV. We associate the observed Fermi surface crossings with the crossing of the strongly hybridized chain/antibonding plane state predicted along ΓX at $k_z\approx\pi$ in the LDA calculations. However, because we do not know the exact value of the inner potential, it is impossible to place strict constraints on the value of k_z which corresponds to any particular photon energy. This is also consistent with the decreased splitting of the plane states at Γ seen for $h\nu=21$ and 28 eV being the result of sampling at different k_z values. Despite the presence of strong correlation effects, the Luttinger theorem anticipates that mean-field calculations within the LDA should still give reasonable predictions for the Fermi-surface topology.

The E vs $\mathbf{k}$ dispersion relations measured along the ΓX high-symmetry line are plotted in Fig. 8. At high binding energy we see a weakly dispersive feature rising from 0.53 eV at Γ to 0.43 eV at X. While, based solely on its dispersion, it could be argued that this feature has chainlike behavior, it is clear from its polarization dependence that this is not plausible, making the most sensible attribution that of the bonding σ state of the cuprate plane bilayer. These bonding (σ) plane bands are expected to be essentially nondispersive parallel to both ΓX and ΓY based on LDA calculations of the band structure, further supporting attribution of this structure to the planes. The quasiparticle originating at lower binding energy at Γ disperses upward toward the Fermi energy, showing a tendency to flatten out just below E_F in the 28 eV data, but exhibiting a clear crossing in the vicinity of the 60% point for $h\nu=21$ eV. From the discussion above, this behavior is consistent with a hybrid band arising from mixing of the antibonding plane and chain states. In the $\mathbf{k}$-space region near X, the weakly dispersing shoulder, at an energy of 0.13 eV, forms a van Hove singularity qualitatively similar to that seen in Bi2212. The data taken with 21 eV photons also shows significant dispersion of the higher binding energy band, suggesting a band of mixed bonding and antibonding character.

Figure 9 plots the measured quasiparticle dispersions along the XS direction. Panels 9(a) and 9(b) show the previ-

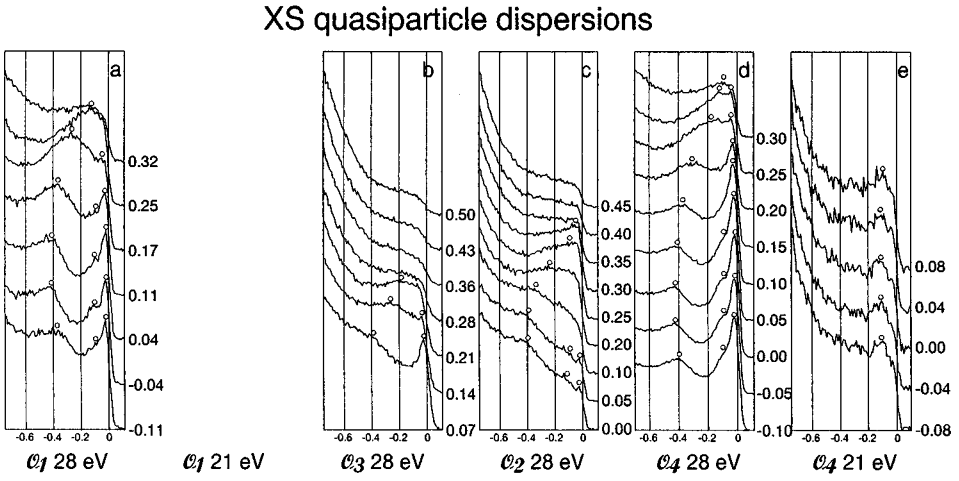

FIG. 9. Energy distribution curves along the XS symmetry line, plotted as in Fig. 5.

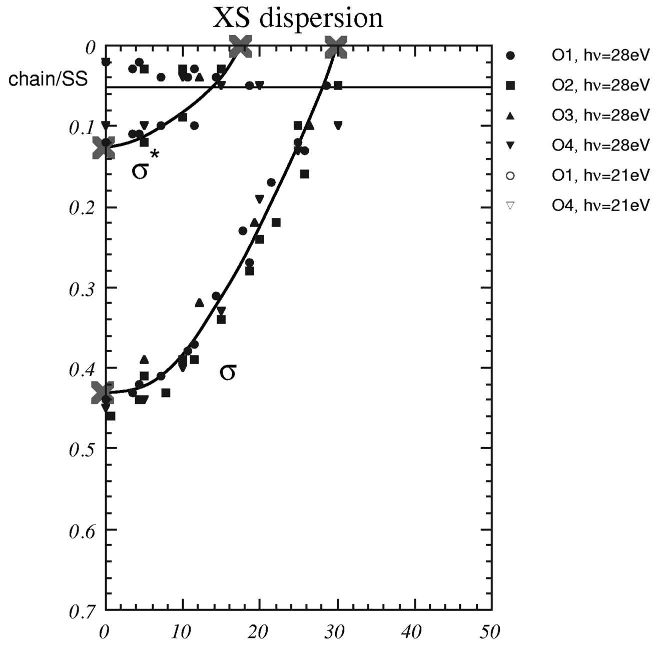

FIG. 10. Energy dispersion of quasiparticles along the XS symmetry line, plotted as in Fig. 6.

ously discussed asymmetry between $\mathcal{O}_1$ and $\mathcal{O}_3$, with the main difference between them being the absence of the shoulder feature at 0.13 eV in the latter. In both, the σ band, with a binding energy of 0.43 eV at X, shows strong upward dispersion through the Fermi energy, crossing around 30% of XS. Weaker upward dispersion is also observed in the $\sigma^\star$ band, which has a crossing near 20% of XS, while the low-energy peak from the chains and/or twinned surface state also disappears in this region of **k** space. The data for chain axis photon polarization [panel 9(c)] show strongly suppressed peak intensities, as would be expected from the matrix elements for plane states, but are otherwise consistent. Similarly, while there is clear enhancement of quasiparticle intensities in $\mathcal{O}_4$ [panel 9(d)], the qualitative behavior is entirely consistent with data from other orientations. Panel 9(e) shows data taken with $h\nu=21$ eV in $\mathcal{O}_4$. The matrix elements are quite weak, but the antibonding band is clearly visible although there is little evidence for the bonding band. As observed along ΓX, the low-energy chain feature is absent in this geometry, presumably due to the k_z dispersion.

Band dispersions along XS are plotted in Fig. 10. Both the bonding σ and antibonding $\sigma^\star$ bands are clearly present, with two corresponding Fermi-surface crossings at 31 and 18% of XS. The fact that the higher binding energy bonding band is not seen in studies of twinned crystals in $\mathcal{O}_2$, as has been the convention in previous work, is significant, particularly as it is this state which reveals anisotropic shifts in the leading edge which mimic the gap behavior in Bi2212, as reported in our previous work.[2]

Figure 11 shows polarization and photon energy-dependent EDC's taken along the ΓY line on the same sample. Spectra taken at 28 eV in $\mathcal{O}_1$ appear in panel 11(a). Like the ΓX spectra for $h\nu=21$ eV, the higher energy feature appearing at 0.53 eV at Γ appears to disperse up toward the Fermi level fairly rapidly, concomitant with the appearance of a second high binding energy quasiparticle, weakly dispersive along ΓY. It appears that these two states become degenerate at Γ. The peak at lower binding energy also disperses upward, as along ΓX, but it is not possible to discern if it crosses the Fermi surface or simply merges with the higher energy peak. By 50% of ΓY, the most prominent feature is an extremely narrow (instrument resolution limited), nondispersive feature which has been attributed by previous authors to an extended van Hove singularity,[19–21] as discussed in the Introduction. Here, we instead interpret this peak as a surface-related chain feature; an extensive discussion of the evidence for this is given below in Sec. VII. Panel 11(c), taken in $\mathcal{O}_3$, also exhibits anomalous intensity discrepancies with spectra in panel 11(a) as with other data taken in this orientation. Nevertheless, the main features are all qualitatively similar. The higher energy peak does not disperse as clearly near Γ, but becomes apparent closer to Y, while the additional quasiparticle seen near 0.65 eV is only visible as a weak hump in the spectra. Spectra at 43 and 50% of ΓY clearly show that the peak nearest E_F is not degenerate with the higher energy feature. Instead, the higher energy state forms a shoulder at around 0.12 eV similar in intensity and dispersion to the $\sigma^\star$ band found along ΓX. Data for polarization parallel to the chains [panel 11(d)] shows significant

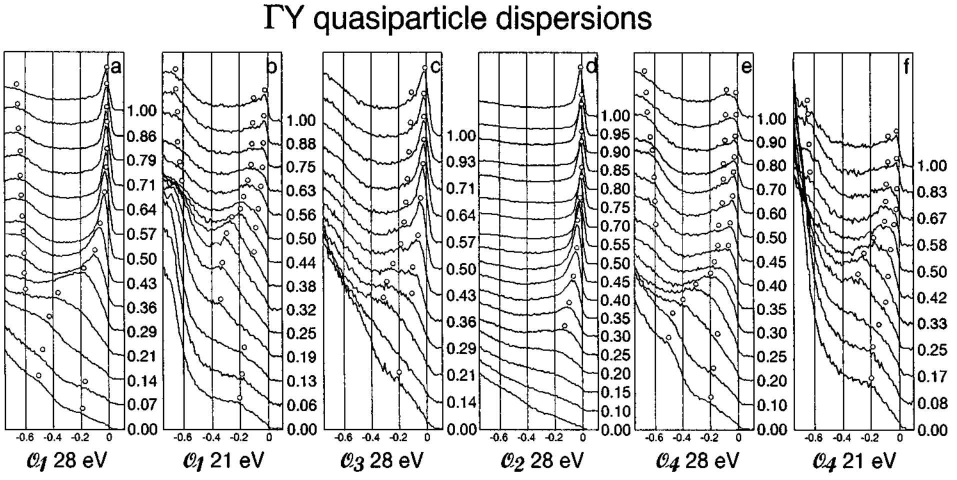

$\mathcal{O}_1$ 28 eV $\mathcal{O}_1$ 21 eV $\mathcal{O}_3$ 28 eV $\mathcal{O}_2$ 28 eV $\mathcal{O}_4$ 28 eV $\mathcal{O}_4$ 21 eV

FIG. 11. Energy distribution curves along the ΓY symmetry line, plotted as in Fig. 5.

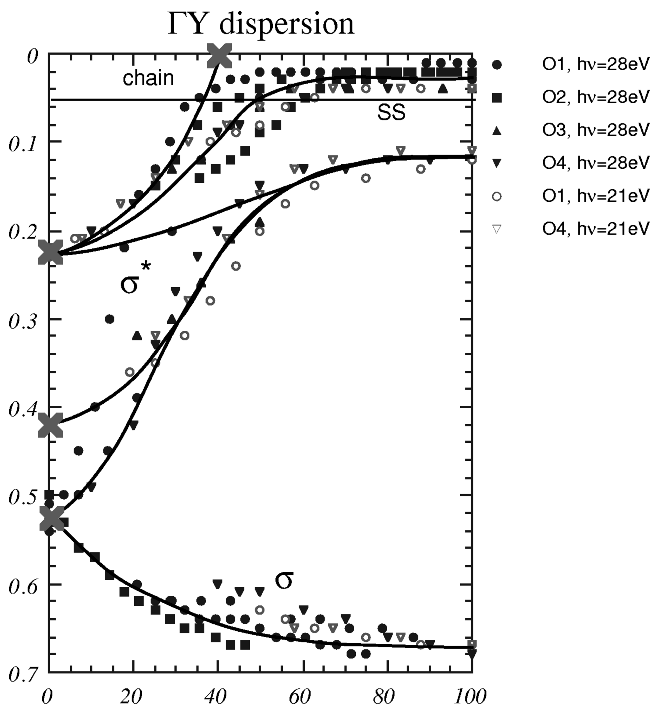

FIG. 12. Energy dispersion of quasiparticles along the ΓY symmetry line, plotted as in Fig. 6.

enhancement of the flat band near the Fermi energy relative to all other spectral features, again supporting the contention that this feature arises principally from the chains. No other quasiparticles are clearly discernible in these EDC's. In contrast, panel 11(e) shows spectra taken with polarization perpendicular to the chains. This data shows the bonding band hybridizing with the antibonding band and dispersing upward, with weak indications of the antibonding band at 0.2 eV. By around 40% of the ΓY distance the hybrid band is seen to merge with the antibonding feature and remain nondispersive at around 0.12 eV to the zone boundary, while a lower binding energy feature also appears and remains at low binding energy. It is likely that this comes from overlap of the hybrid chain-antibonding plane band and the surface state discussed below. Also visible at higher energy is the nondispersive peak around 0.65 eV, which appears consistent with the bonding plane σ band, shifted down in energy by the chain-induced anisotropy.

The spectra taken with 21 eV photons are presented in panels 11(b) and 11(f). Both panels show substantially similar features, with a band originating at a slightly lower energy of 0.42 eV than for $h\nu = 28$ eV due to the c-axis dispersion. This band then moves to lower energies, and flattens out to form the expected plane band van Hove singularity, the nondispersive band lying at 0.12 eV binding energy near Y. A flat band associated with the surface chain feature appears at even lower binding energy, although with significantly reduced intensity. The dependence of the surface chain feature on photon energy is extensively discussed in Sec. VII B.

The dispersion relations for ΓY are plotted in Fig. 12. While the presence of the surface feature complicates the data somewhat, presented in this way there is actually quite a large degree of consistency with the data along ΓX. The bonding σ band appears at around 0.53 eV at Γ and disperses weakly downward to 0.67 eV at Y. A second band disperses upward to merge with the pure antibonding $\sigma^\star$ state in a van Hove singularity with 0.12 eV binding energy at Y. The observed dispersion seems to be consistent with the expected chain Fermi-surface crossing appearing near 40% of ΓY, at which point the surface chain feature becomes prominent at very low binding energy.

Angle-resolved spectra along YS are presented in Fig. 13. In general the signal is dominated by the contribution of the narrow surface chain feature, with a photon polarization component parallel to the chains in $\mathcal{O}_1$, $\mathcal{O}_2$, and $\mathcal{O}_3$. The details of the polarization dependence are treated below (Sec. VII); here we simply note that the greatest intensity is seen in $\mathcal{O}_2$ for which the polarization lies entirely along the b axis. Orientations $\mathcal{O}_1$ and $\mathcal{O}_3$ both show the feature diminished in intensity relative to the incoherent spectral weight, and a higher energy shoulder can be clearly resolved at 0.12 eV in the former, while the latter shows some asymmetrical broadening compared with $\mathcal{O}_2$. Panels 13(d) and 13(e), taken with

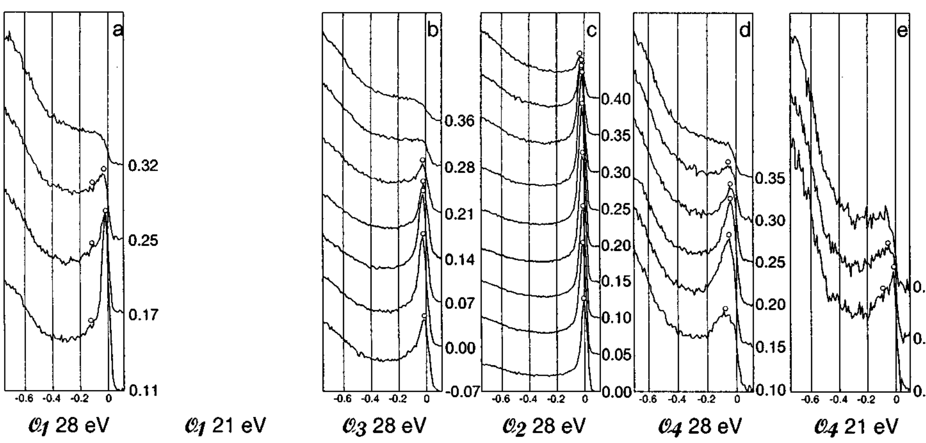

$\mathcal{O}_1$ 28 eV $\mathcal{O}_1$ 21 eV $\mathcal{O}_3$ 28 eV $\mathcal{O}_2$ 28 eV $\mathcal{O}_4$ 28 eV $\mathcal{O}_4$ 21 eV

FIG. 13. Energy distribution curves along the YS symmetry line, plotted as in Fig. 5.

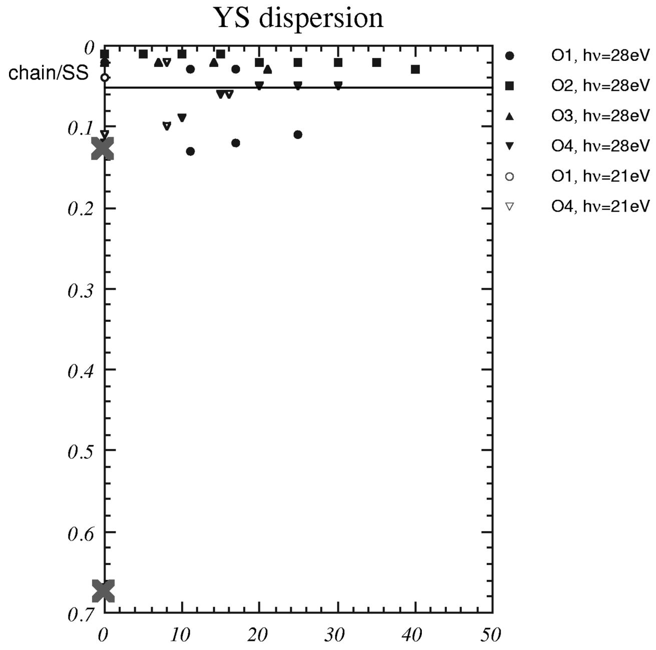

FIG. 14. Energy dispersion of quasiparticles along the YS symmetry line, plotted as in Fig. 6.

polarization perpendicular to the chains, are qualitatively different, with the quasiparticle features being much broader, and lying at the same energy as the shoulder seen in $\mathcal{O}_1$. The dispersion curves corresponding to these EDC's are plotted in Fig. 14.

VI. TIGHT BINDING BANDS

Quantitative calculations of various transport and optical properties require accurate information on details of band structure. To facilitate such endeavors, we have fit our dispersion curves along the ΓS, ΓX, and XS high-symmetry lines using the tight-binding basis of Norman *et al.*,[31] which they applied to fitting the band structure of Bi2212. Due to the presence of measurable bilayer splitting in Y123, there are two sets of tight-binding parameters, one for the $pd\sigma$ bonding bands and another for the $pd\sigma^\star$ antibonding bands. These are given, along with the corresponding basis functions, in Table II. The two-dimensional crystal momentum dependence of the energy bands within this approximation is then simply given by

$$E(\mathbf{k}) = \sum_i c_i \eta_i(\mathbf{k}). \tag{9}$$

While there does appear to be measureable k_z dispersion in at least the bonding plane bands, our investigations are not sufficiently detailed to allow a quantitative fitting of these to a full three-dimensional dispersion relation. The difficulty of discriminating bulk bands in the $\Gamma YS\Gamma$ octant prevents easy quantitative assessment of the degree of coupling between the chains and planes, so we have not attempted to address this issue here, even though the $pd\sigma$ band is visible along ΓY in some experimental geometries and the $pd\sigma^\star$ band manifests behavior quantitatively similar to that along ΓX.

TABLE II. Tight-binding basis functions and best-fit parameters for the measured bonding and antibonding band dispersions in Y123. Least-squares fitting was performed for bands along the ΓS, ΓX, and XS high-symmetry lines, and did not include the symmetry-breaking effects of the chains.

$\eta_i(\mathbf{k})$	$c_i^{pd\sigma}$	$c_i^{pd\sigma^\star}$
1	0.1756	0.4368
$\frac{1}{2}(\cos k_x + \cos k_y)$	-1.1259	-1.0939
$\cos k_x \cos k_y$	0.5540	0.5612
$\frac{1}{2}(\cos 2k_x + \cos 2k_y)$	-0.1774	-0.0776
$\frac{1}{2}(\cos k_x \cos 2k_y + \cos 2k_x \cos k_y)$	-0.0701	-0.1041
$\cos 2k_x \cos 2k_y$	0.1286	0.0674

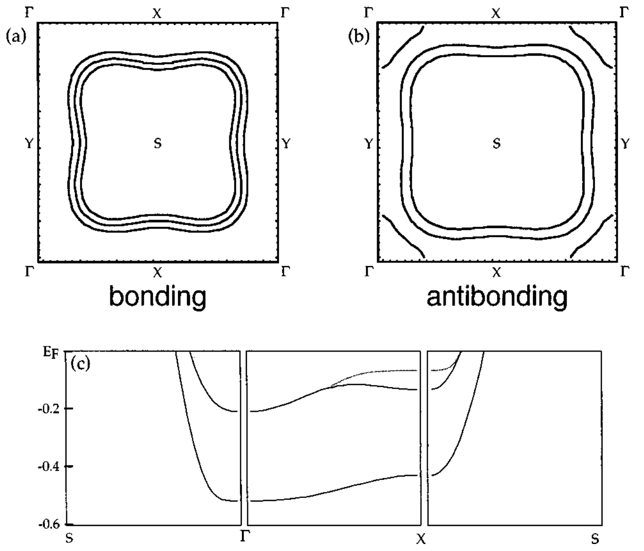

FIG. 15. Results of a tight-binding least squares fit to our measured ARPES band dispersions along the ΓS, ΓX, and XS high-symmetry lines. Panels (a) and (b) show the Fermi surfaces (middle contour) for the bonding and antibonding bands, respectively, and contours corresponding to energies of $E_F \pm 150$ meV. Tight-binding band dispersions are shown in panel (c) for the high-symmetry lines. Uncertainty in the exact binding energy of the antibonding band due to overlap with the chain feature near E_F is indicated by the presence of grayed bands near X.

Figure 15 presents the Fermi surfaces and band dispersions resulting from our tight-binding fit. Panels 15(a) and 15(b) show the Fermi surface and contours corresponding to 150 meV above and below the Fermi energy for the bonding and antibonding bands, respectively. As expected, the bonding Fermi surface is well-localized in **k** space and is weakly dispersive. In contrast, the antibonding pocket reveals large sections of the Brillouin zone having weight near the Fermi energy, corresponding to the flat plane bands near X/Y. Because of the contaminating effects of the strong feature at Y (see discussion in Sec. VII), the exact energy position of the van Hove singularity in the antibonding plane band is difficult to determine precisely. The best-fit tight-binding bands themselves are plotted in panel 15(c).

VII. SURFACE CHAIN FEATURE

In order to firmly establish the asymmetric character of the surface chain feature (SCF), we examined a cleaved, untwinned crystal with unpolarized Ne I radiation (16.85 eV),

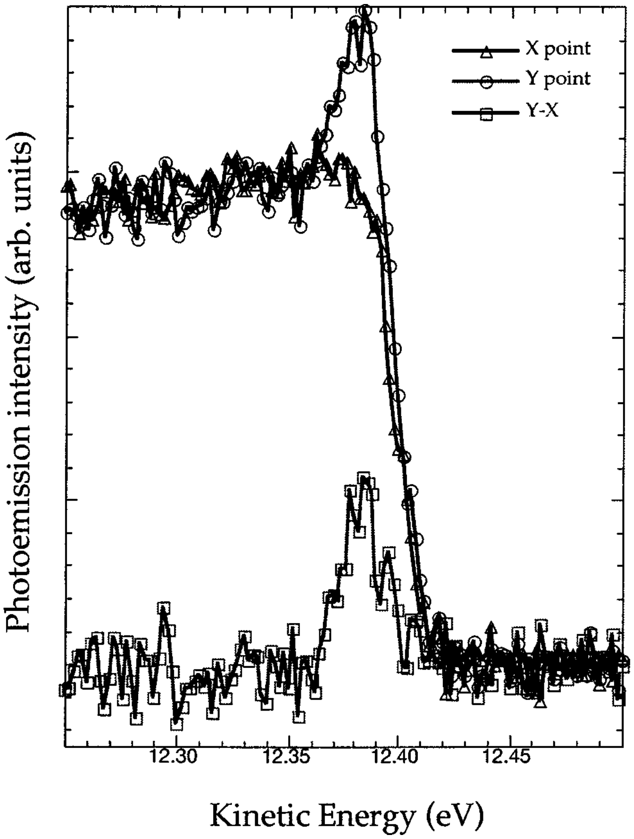

FIG. 16. Spectra taken with unpolarized Ne I radiation (16.85 eV) at the *X* and *Y* points, revealing the presence of the SCF at *Y* and its absence at *X*. The difference spectrum reveals that the underlying electronic structure of the two is quite similar except for the narrow peak near E_F. Overall instrumental resolution for this data is ≈20 meV.

in a geometry where all external experimental conditions were identical for spectra taken at both *X* and *Y*. The resulting EDC's are presented in Fig. 16, along with their difference, definitively demonstrating that the asymmetry is real and independent of photon polarization and geometry. Furthermore, we can see that, aside from the extremely narrow feature at E_F (instrument resolution limited at approximately 20 meV), the two **k** points are quite similar.

The presence of a feature at the *Y* point, absent at *X*, does not of itself imply chain parentage (due to the orthorhombic distortion of the underlying lattice), but the extremity of the asymmetry and apparently one-dimensional behavior are difficult to reconcile with the 2D planar structure of the CuO$_2$ sheets. Also difficult to understand, assuming that the orthorhombic distortion is responsible for the asymmetry, is the nondispersive nature of the SCF with photon energy. A number of additional arguments, delineated below, provide strong support for the contention that the SCF is indeed derived from the CuO$_3$ chains.

A. Polarization dependence

Figure 17 shows ARPES EDC's taken at the *X* and *Y* points, with $h\nu=28$ eV, for the three distinct polarization geometries; panel (a) corresponding to $\mathbf{E}\parallel b$, panel (b) to $\mathbf{E}\perp b$, and panel (c) to $\mathbf{E}\parallel\Gamma S$ (orientations $\mathcal{O}_2$, $\mathcal{O}_4$, and $\mathcal{O}_1$, respectively). It is important to recognize that, while the absolute value of the intensity axis is not significant, the relative amplitudes between spectra are, as they are scaled to the integrated valence-band emission, and may be compared qualitatively. To the extent that the chains are truly one-dimensional, the photoemission spectra taken with photon polarization parallel to the *b* axis should maximize their contribution to the signal, those with perpendicular polarization should be essentially free of chain signal, and those with intermediate polarization should mix the two. Contrasting with this, the predominantly $d_{x^2-y^2}$ Cu 3*d* states hybridized with O 2*p* states to form the plane bands constituting the near E_F structure should be comparatively unaffected by the 90° rotation, other than experiencing slight asymmetry due to the orthorhombic structure and the normal selection rule effects for electron emission.

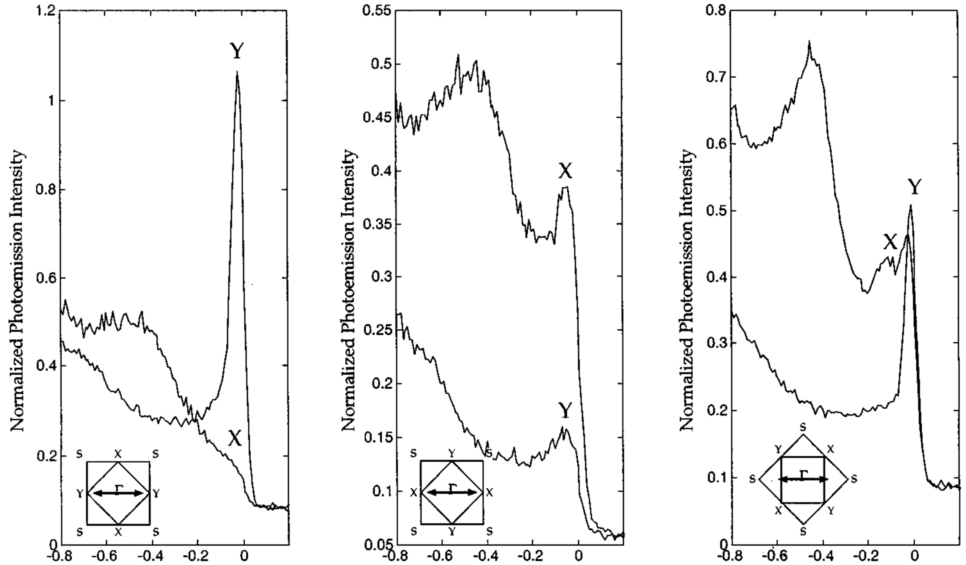

FIG. 17. Photoemission EDC's taken at the *X* and *Y* points of a single sample, for photon polarization $\mathbf{E}\parallel b$ (a), $\mathbf{E}\perp b$ (b), and $\mathbf{E}\parallel\Gamma S$ (c).

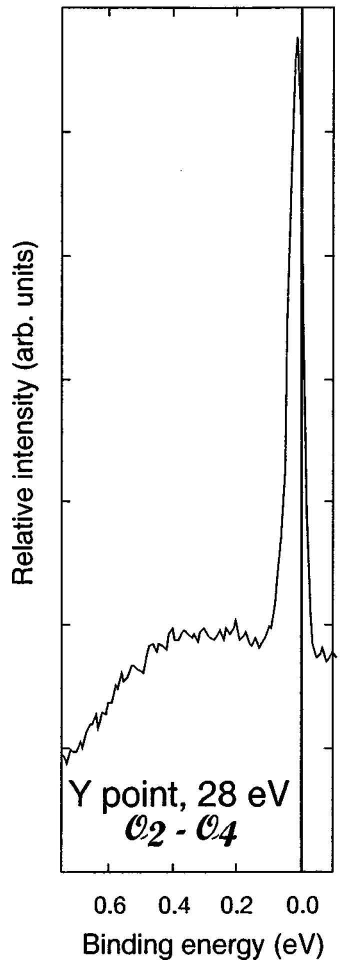

FIG. 18. Normalized difference spectrum for spectra taken at the *Y* point with photon polarization parallel and perpendicular to the CuO_3 chains.

Examination of the spectra at *Y* dramatically demonstrates the dependence of the SCF on sample orientation; the spectrum with $\mathbf{E}\|\Gamma Y$ shows enormous enhancement, while the perpendicular geometry reveals nearly complete suppression, and the 45° spectrum shows almost exactly half the intensity of that in $\mathcal{O}_2$, as expected from geometrical arguments. Furthermore, in addition to its factor of eight diminishment in intensity, the small residual peak seen at *Y* in $\mathcal{O}_4$ is qualitatively unlike the SCF, being much broader and lying at measurably higher binding energy, and presumably originates in the planes. This quasiparticle behaves in a manner qualitatively similar to that seen in Bi2212. A third feature of the electronic structure, which appears weakly as an extremely broad peak at a binding energy of 650 meV, is essentially unaffected by the polarization component parallel to the chains so it must also derive from the underlying CuO_2 plane states. Also important is the comparatively weak dependence of the overall intensity away from E_F on geometry, all three EDC's at *Y* lying between 0.25 and 0.45 at the high binding energy limit.

In Fig. 18 we plot the difference between normalized spectra at the *Y* point in the geometry in which polarization is parallel to the chains and that in which it is perpendicular to them. What is observed strikingly confirms our arguments above; the only significant difference between the two in the 0.5 eV below the Fermi energy lies in the narrow peak lying at a binding energy of 13 meV, as reported in previous studies of the evHs in Y123, and with a width which is almost entirely comprised of the instrument contribution. It is important to note that the two spectra used were taken on the same sample, with the only difference between the two being the photon polarization relative to the chains. The extreme narrowness of this feature is in stark contrast with the other dispersive bands seen on the same sample, all of which are broader by a factor of 10–20. By this coexistence of both very narrow and very broad features in the photoemission spectra from one sample we are able to infer that the broad peaks are intrinsic in origin, and do not stem from poor sample quality or energy resolution.

Turning to the spectra at *X*, we immediately note the absence of any features in the near-E_F weight of comparable intensity to the SCF in any polarization orientation. As for the *Y* point, the high binding energy intensities are only weakly dependent on geometry, although the matrix elements at *X* appear to lead to overall enhancement for emission from this region of $\mathbf{k}$ space. Also as seen at *Y*, a broad higher binding energy feature (around 400 meV) with little dependence on the chain component of $\mathbf{E}$ is found. It is important to also consider the (likely) scenario of residual twinning of the crystals at the few percent level, as the detwinning procedure is never entirely perfect. In the case of a lightly twinned crystal, the intense feature near *Y* will be mirrored at *X*, albeit with its intensity significantly reduced. Nevertheless, because this structure is so intense in the parallel polarization geometry, even a few percent can cause a significant and spurious addition of spectral weight in the energy region immediately below E_F.

B. Photon energy dependence

Another aspect of the photoemission data on this compound which has been puzzling is the strong photon energy dependence of the SCF intensity. From the experimentally measured dispersion relations, the binding energy of this state exhibits little dependence on $\mathbf{k}$. Given a nondispersive initial state and further assuming a three-dimensional free-electron-like final state, we can model the situation in a simple way in terms of direct transitions within the three-step model. Since the parallel components of $\mathbf{k}$ are conserved in the photoemission process, we can write the final-state energy as

$$E_f=\frac{\hbar^2}{2m_e}\left[\left(\frac{\pi}{a}k_x,\frac{\pi}{b}k_y,\frac{\pi}{c}k_z\right)+\left(\frac{2\pi}{a}l,\frac{2\pi}{b}m,\frac{2\pi}{c}n\right)\right]^2-\Phi_0. \tag{10}$$

For the SCF we have $(k_x,k_y,k_z)=(0,1,k_z)$, so this reduces to

$$h\nu-W+\Phi_0=\left(\frac{1}{2m_e}\right)\hbar^2\left(\frac{\pi}{b}^2(1+2m)^2+\frac{\pi}{c}^2(k_z+2n)^2\right). \tag{11}$$

We use a work function $W=5$ eV based on the work of Rietveld *et al.*,[32] a b-axis lattice constant of 3.86 Å, a c-axis lattice constant of 11.7 Å, and further assume that the tran-

TABLE III. Photon energies for which enhanced photoemission intensities from the feature at the Y point are predicted to be maximized, using a simple free-electron final-state model and assuming strictly two-dimensional character.

n	$h\nu$	n	$h\nu$
2	1.5 eV	7	57 eV
3	8 eV	8	74 eV
4	17 eV	9	94 eV
5	28 eV	10	116 eV
6	41 eV		

sitions at 17 and 28 eV are separated by a single c-axis reciprocal-lattice vector, $G_z = 2\pi/c$, to determine n:

$$17-5+\Phi_0=0.275(k_z+2n)^2+2.580(1+2m)^2, \quad (12)$$

$$28-5+\Phi_0=0.275[k_z+2(n+1)]^2+2.580(1+2m)^2. \quad (13)$$

Solving these two equations gives two possible integral values: $n=4,5$, corresponding to $k_z=\pm\pi/c$. These values precisely correspond to parts of the Brillouin zone where the k_z dispersion of the initial-state bands would be stationary, thus making a large contribution to the density of states. From this, we may in turn estimate the inner potential, although this requires assuming some value for m which we take to be zero. Then, we find that $\Phi_0 \approx 12.9$ eV. This seems to be a perfectly reasonable value; for comparison, Manzke *et al.*[33] report a value of 10 eV for TaS_2. Using this we can predict other photon energies where there should be significant photoemission intensity by solving Eq. (11); values for $n \leqslant 10$ are given in Table III. Previous studies have found evidence for the SCF at 74 eV (Ref. 16) and 94 eV,[34] while we have observed a peak at $h\nu=42$ and 57 eV. Comparison of the energies where peaks are seen experimentally with the tabulated predictions reveals excellent agreement for $4 \leqslant n \leqslant 9$.

C. Oxygen doping dependence

In Y123, oxygen doping is known to affect only the oxygen stoichiometry of the chains, which act as a charge reservoir for hole doping of the planes, while leaving the planar structure unaltered. As vacancies are introduced, the long-range order of contiguous CuO_3 chains is broken, leaving chain segments of decreasing length, although the microscopic effects of deoxygenation have not been unambiguously determined. In the fully deoxygenated limit, $\delta=1$ ($YBa_2Cu_3O_6$), the CuO_3 chains have been completely replaced by CuO_2 dimers. In the intermediate oxygen doping regime, $0<\delta<1$, vacancies are gradually incorporated into the chains. The ortho-II ordering transition, which occurs at $\delta=0.5$,[35] and has been associated with the observed plateau in T_c with δ, leads to vacancies preferentially occupying alternate rows, leaving the remaining chains intact. In their photoemission study of oxygen doping, Liu *et al.* found that the peak near Y was clearly present, with diminishing intensity, down to a composition of $\delta=0.5$, but vanished abruptly below this value.[14] Within the context of our model and in light of the existence of the ortho-II transition, we expect precisely this behavior for a chain-derived state which can only exist in doping regimes where contiguous chains having long-range structural order are present. Once significant numbers of vacancies are introduced into the remaining chains, decreasing their average lengths, any states originating in them will disappear.

TABLE IV. Intensity ratios for the surface chain feature at the Y point from various samples of Y123 and Y124. UBC indicates samples from the University of British Columbia, UMD indicates samples from the University of Maryland, and Argonne indicates published results from that group's work on twinned Y123 and untwinned Y124.

Sample	R_p
Y123 (twinned) UMD	2.3
$YPr_{0.05}123$ (twinned) UMD	2.2
$YPr_{0.22}123$ (twinned) UMD	2.1
Y123 X III (untwinned) UBC	4.9
Y123 X II (untwinned) UBC	4.0
Y123 X V (untwinned) UBC	5.3
Y123 X VII (untwinned) UBC	4.5
Y123 X III 2 (untwinned) UBC	4.8
Y123 (untwinned) $\delta=6.5$ Argonne	3.6
Y124 (untwinned) Argonne	9.6
Y124 (untwinned) Argonne	7.4

D. Peak intensity ratio

The absence in Bi2212 of a feature comparable in width and anisotropy to the SCF provides an additional clue; the extended flat band in the Bi compound exhibits substantially greater dispersion, is observed symmetrically along both of the cubic axes, and is much broader than the SCF in Y123.[36] Conversely, a similar SCF feature, with even greater intensity, is found in Y123's sister compound, Y124;[20] the peculiarity of the SCF to compounds possessing CuO_3 chains is itself highly suggestive. In Table IV we compare the relative peak to background ratio, R_p (defined as the ratio of the peak height at Y to the incoherent spectral weight 0.2 eV below E_F), from various twinned and untwinned samples of Y123 and Y124. Taking into account the inevitable sample to sample variation, R_p in untwinned Y123 is seen to be roughly twice that of twinned samples, with untwinned Y124 being twice again as large.

This variation is easily explained by two facts. First, in a twinned sample the intensity from the Y point will be evenly distributed between X and Y. Second, as previously discussed, the principal structural distinction of the Y124 material is that it contains twice as many chains per unit cell and is naturally (partially) untwinned;[17] it is expected that the cleaved surface should have a similarly disproportionate number of exposed chains, leading to an enhancement factor of 2 in samples with uniform cleavage planes. The specific ratio will, of course, depend on the sample and is expected to exhibit cleave-to-cleave variation due to differences in the BaO/CuO_3 distribution at the interface.

E. Doping dependence

Investigations of heavily Co-doped, twinned crystals of Y123 by Gu *et al.*,[16] in which the Co substitutes exclusively for the chain Cu(1), revealed essentially no effect on the ΓS quasiparticle features for superconducting crystals with Co doping as high as 18%. This data supports the contention that the pair of quasiparticles observed along this line arises principally from the CuO_2 planes, having a small chain-state contribution. Unfortunately, to the best knowledge of the authors, there are no published spectra from these crystals at the zone boundary near the equivalent X/Y points, where we expect effects on the electronic structure due to chain disruption by Co should be the strongest.

Finally, Pr doping, which substitutes Pr for the interplane Y atom, has the unique property among the substitutional rare earths of strongly suppressing the superconductivity of $Y_{1-x}Pr_xBa_2Cu_3O_{7-\delta}$ (YPr123), inducing a metal-insulator transition at a Pr concentration of $x \approx 0.55$. Because the Pr atom lies between the CuO_2 planes and is quite isolated from the chains, it would be expected to have a comparatively large effect on plane-derived states and to only weakly affect chain features. In studies of twinned crystals of YPr123,[37] we find that the most dramatic changes in the electronic structure at low doping are observed along the ΓS line, the main feature of which derives predominantly from plane states and is unaffected by the twinning. In contrast, the SCF is clearly present, even for $x = 0.22$, where T_c has been suppressed to 60 K. Our results strongly mimic changes observed in the near E_F features of oxygen deficient samples, indicating that Pr alters the relative charge balance between chains and planes, but does not affect the presence of the SCF at moderate doping levels.

Taken together, we believe that this evidence provides a consistent and compelling case for association of the SCF with a surface chain state which is uncharacteristic of the bulk electronic structure of Y123, and which, by virtue of its intensity and proximity to the Fermi energy, strongly masks the presence of any underlying states or gaps in the **k**-space region near the Y point. Furthermore, except under the most favorable conditions and with almost perfectly detwinned samples, highly intense echoes of the SCF will appear near E_F at the X point as well, contaminating data from this region as well.

VIII. EVIDENCE FOR BILAYER SPLITTING

Bilayer splitting, which arises from bonding-antibonding pairing of interplane wave functions, is predicted to be approximately 0.75 eV at Γ in Y123, substantially larger than that expected in Bi2212. Some theoretical predictions, principally based on the short c-axis mean free paths in normal-state transport data, have argued that the conductivity data fundamentally contradict bandlike behavior along this axis, thus precluding the possibility of this splitting.[38] In particular, the interlayer tunneling mechanism of high-temperature superconductivity relies on incoherence of the interbilayer transport in the normal state. For this reason, it is important to critically evaluate the evidence for this splitting in Y123 and discuss its significance. The hallmark of bilayer splitting is the appearance of two nondegenerate bands arising from the CuO_2 planes, while a degeneracy of these bands might be, but is not necessarily, an indication of non-Fermi-liquid behavior. While our data are taken in the superconducting state, the vastly different energy scales for the expected splitting and the superconductivity-induced modifications in the electronic structure make it unlikely that this is a relevant consideration.

As extensively discussed in Sec. V, our data clearly reveal two plane-derived quasiparticle features which have binding energies of 0.22 and 0.53 eV at Γ for $h\nu = 28$ eV, with the higher energy peak showing at least 0.12 eV dispersion along the c axis. In contrast, there is no apparent c-axis dispersion of the low binding energy feature in our data. These features disperse weakly upward toward X, appearing at 0.13 and 0.43 eV, respectively, and exhibit Fermi-surface crossing behavior agreeing well with qualitative aspects of LDA calculations. On the basis of this evidence, it appears that these features are in fact the expected bilayer split plane states, with the magnitude of the splitting diminished by roughly a factor of 2 from its calculated value, presumably due to correlation effects.

The apparent observation of bilayer splitting and c-axis dispersion in Y123 raises some intriguing questions regarding the qualitative disagreement between high-energy measurements such as photoemission and low-energy measurements such as transport. In most of the cuprates, the c-axis mean free path for electron transport is shorter than the lattice constant in that direction, making it plausible to argue that the transport in this direction is incoherent.[38] However, this conclusion, based on the results of transport measurements at very small energy scales, does not necessarily imply that high-energy spectroscopies such as photoemission should not see fundamentally different effects.[39] In fact, the observation of bilayer splitting and c-axis dispersion in Y123 points to the need for a conceptual distinction between the two very different energy scales probed by these different techniques. Such a duality in which bandlike dispersive quasiparticles are seen in photoemission measurements of materials which are clearly insulating in transport has been seen in a number of other systems including NiO,[40] $Sr_2CuO_2Cl_2$,[30] and other Mott insulators.

IX. SUMMARY AND CONCLUSIONS

In summary, extensive studies of the dispersive quasiparticle states in optimally doped untwinned single crystals of Y123 using polarization-dependent angle-resolved photoelectron spectroscopy have illuminated a number of points regarding the electronic structure of this material. Based on analysis of the Ba $5p$ core level and inference from other surface-sensitive probes, we are able to reproduce the observed surface to bulk intensity ratio with a simple model incorporating a mixed surface termination of BaO and CuO_3 regions. Furthermore, we find the electron attenuation length in this material to be approximately 5 Å, consistent with the so-called ''universal'' curve. Due to the large dimension of the unit cell along the c axis (more than twice the attenuation length), the bulk of the photoemission intensity will arise from the surface planes and the first subsurface CuO_2 planes, with significant attenuation of the signal from the bulk chains. We also observe a measurable anisotropy between the peak observed at 1 eV binding energy at the X and Y points.

Extensive arguments, based on photon polarization dependence, photon energy dependence, intensity variations between twinned, untwinned, and Y124 crystals, and oxygen, Co, and Pr doping results, are presented in favor of attribution of the intense, narrow feature found near the Y point to a surface-related chain state. This feature, which appears at both X and Y in twinned crystals, is extrinsic to the bulk electronic states of Y123, and contaminates data in the crucial near E_F region in crystals which are not exceptionally well detwinned.

The measured band dispersions clearly reveal two plane-derived quasiparticle states, one with a binding energy of 0.22 eV at Γ, and the other at 0.53 eV, which we associate with the antibonding and bonding bilayer bands. The former disperses upward to form a van Hove singularity with a binding energy of 0.13 eV at X, while the latter is weakly dispersive along ΓX, and disperses rapidly upward along XS. While no measurable c-axis dispersion is seen in the antibonding band by changing the photon energy, the bonding band shifts upward by 0.11 eV when $h\nu$ is changed from 28 to 21 eV. Observation of two distinct plane states and c-axis dispersion provides clear evidence for bilayer splitting in Y123, consistent with the simplest band-theoretical arguments. The clear disagreement of these measurements with the results of low-energy transport measurements emphasizes the importance of interaction between the characteristic energies of the physical phenomena and of the experimental probe.

ACKNOWLEDGMENTS

The data in this study were obtained at the Stanford Synchrotron Radiation Laboratory (SSRL) which is operated by the DOE Office of Basic Energy Sciences, Division of Chemical Sciences. The Office's Division of Materials Science has also provided support for this study. The Stanford work was supported through ONR Grant No. 00014-95-1-0960, and the Center for Materials Research. D.A.B., R.L., and W.N.H. acknowledge the support of the Natural Science and Engineering Research Council of Canada, and the Canadian Institute for Advanced Research. The authors would like to thank Professor Rick Greene and Dr. J. L. Peng for providing twinned crystals of Pr-doped Y123, Dr. Warren Pickett for unpublished results from some of his calculations, Dr. Glenn Waychunas for assistance with the x-ray-diffraction measurements, Dr. Changyoung Kim and Dr. Tony Loeser for assistance with data acquisition, and Professor R. B. Laughlin, Professor S. Doniach, Professor S. Kivelson, Professor M. Norman, Professor P. W. Anderson, and Dr. Tony Loeser for many helpful discussions. M.C.S. gratefully acknowledges the support of the Fannie and John Hertz Foundation.

---

[1] Z.-X. Shen, D.S. Dessau, B.O. Wells, D.M. King, W.E. Spicer, A.J. Arko, D.S. Marshall, L.W. Lombardo, A. Kapitulnik, P. Dickinson, S. Doniach, J. DiCarlo, A.G. Loeser, and C.H. Park, Phys. Rev. Lett. **70**, 1553 (1993).

[2] M.C. Schabel, C.-H. Park, A. Matsuura, Z.-X. Shen, D.A. Bonn, R. Liang, and W.N. Hardy, Phys. Rev. B **55**, 2796 (1997).

[3] B.W. Veal and C. Gu, J. Electron Spectrosc. Relat. Phenom. **66**, 321 (1994).

[4] D.J. van Harlingen, Rev. Mod. Phys. **67**, 515 (1995).

[5] D.A. Bonn and W.N. Hardy, in *Physical Properties of High-Temperature Superconductors*, edited by D. Ginsberg (World Scientific, Amsterdam, 1996), Vol. V, Chap. 9.

[6] J.R. Kirtley, C.C. Tsuei, J.Z. Sun, C.C. Chi, L.S. Yu-Jahnes, A. Gupta, M. Rupp, and M.B. Ketchen, Nature (London) **373**, 225 (1995).

[7] Z.-X. Shen and D.S. Dessau, Phys. Rep. **253**, 1 (1995).

[8] H.L. Edwards, J.T. Markert, and A.L. de Lozanne, Phys. Rev. Lett. **69**, 2967 (1992).

[9] W.E. Pickett, R.E. Cohen, and H. Krakauer, Phys. Rev. B **42**, 8764 (1990).

[10] O.K. Andersen, A.I. Liechtenstein, C.O. Rodriguez, I.I. Mazin, O. Jepsen, V.P. Antropov, O. Gunnarsson, and S. Gopalan, Physica C **185-189**, 147 (1991).

[11] O.K. Andersen, O. Jepsen, A.I. Liechtenstein, and I.I. Mazin, Phys. Rev. B **49**, 4145 (1994).

[12] J.C. Campuzano, G. Jennings, M. Faiz, L. Beaulaigue, B.W. Veal, J.Z. Liu, A.P. Paulikas, K. Vandervoort, H. Claus, R.S. List, A.J. Arko, and R.J. Bartlett, Phys. Rev. Lett. **64**, 2308 (1990).

[13] R. Liu, B.W. Veal, A.P. Paulikas, J.W. Downey, H. Shi, C.G. Olson, C. Gu, A.J. Arko, and J.J. Joyce, Phys. Rev. B **45**, 5614 (1992).

[14] R. Liu, B.W. Veal, A.P. Paulikas, J.W. Downey, P.J. Kostić, S. Fleshler, U. Welp, C.G. Olson, X. Wu, A.J. Arko, J.J. Joyce, Phys. Rev. B **46**, 11 056 (1992).

[15] J.G. Tobin, C.G. Olson, C. Gu, J.Z. Liu, F.R. Solal, M.J. Fluss, R.H. Howell, J.C. O'Brien, H.B. Radousky, and P.A. Sterne, Phys. Rev. B **45**, 5563 (1992).

[16] C. Gu, B.W. Veal, R. Liu, H. Ding, A.P. Paulikas, J.C. Campuzano, P. Kostić, R.W. Wheeler, H. Zhang, C.G. Olson, X. Wu, and D.W. Lynch, J. Phys. Chem. Solids **54**, 1177 (1993).

[17] J.-C. Campuzano, K. Gofron, R. Liu, H. Ding, B.W. Veal, and G. Dabrowski, J. Phys. Chem. Solids **53**, 1577 (1992).

[18] A. Shukla, L. Hoffmann, A.A. Manuel, E. Walker, B. Barbiellini, and M. Peter, Phys. Rev. B **51**, 6028 (1995).

[19] A.A. Abrikosov, J.C. Campuzano, and K. Gofron, Physica C **214**, 73 (1993).

[20] K. Gofron, J.C. Campusano, H. Ding, C. Gu, R. Liu, B. Dabrowski, B.W. Veal, W. Cramer, and G. Jennings, J. Phys. Chem. Solids **54**, 1193 (1993).

[21] K. Gofron, J.C. Campuzano, A.A. Abrikosov, M. Lindroos, A. Bansil, H. Ding, D. Koelling, and B. Dabrowski, Phys. Rev. Lett. **73**, 3302 (1994).

[22] R.S. List, A.J. Arko, Z. Fisk, S.-W. Cheong, S.D. Conradson, J.D. Thompson, C.B. Pierce, D.E. Peterson, R.J. Bartlett, N.D. Shinn,

J.E. Schirber, B.W. Veal, A.P. Paulikas, and J.C. Campuzano, Phys. Rev. B **38**, 11 966 (1988).

[23] H.L. Edwards, A.L. Barr, J.T. Markert, and A.L. de Lozanne, Phys. Rev. Lett. **73**, 1154 (1994).

[24] J. Halbritter, P. Walk, H.-J. Mathes, W. Aarnink, and I. Apfelstedt, in *High T_c Superconducting Thin Films, Devices, and Applications*, edited by G. Margaritondo *et al.*, AIP Conf. Proc. No. 182 (AIP, New York, 1988), p. 208.

[25] M.P. Seah and W.A. Dench, Surf. Interface Anal. **1**, 1 (1979).

[26] C.G. Olson, J.G. Tobin, G.D. Waddill, D.W. Lynch, and J.Z. Liu, J. Phys. Chem. Solids **56**, 1879 (1995).

[27] R. Claessen, G. Mante, A. Huss, R. Manzke, M. Skibowski, Th. Wolf, and J. Fink, Phys. Rev. B **44**, 2399 (1991).

[28] R. Manzke, G. Mante, M. Skibowski, and J. Fink, Physica C **185-189**, 843 (1991).

[29] J.J.M. Pothuizen, R. Eder, N.T. Hien, M. Matoba *et al.*, Phys. Rev. Lett. **78**, 717 (1997).

[30] B.O. Wells, Z.-X. Shen, A. Matsuura, D.M. King, M.A. Kastner, M. Greven, and R.J. Birgeneau, Phys. Rev. Lett. **74**, 964 (1995).

[31] M.R. Norman, M. Randeria, H. Ding, and J.C. Campuzano, Phys. Rev. B **52**, 615 (1995).

[32] G. Rietveld, N.Y. Chen, and D. van der Marel, Phys. Rev. Lett. **69**, 2578 (1992).

[33] R. Manzke, O. Andersen, and M. Skibowski, J. Phys. C **21**, 2399 (1988).

[34] C.G. Olson (private communication).

[35] P. Schleger, R.A. Hadfield, H. Casalta, N.H. Andersen, H.F. Poulsen, M. von Zimmermann, J.R. Schneider, Ruixing Liang, P. Dosanjh, and W.N. Hardy, Phys. Rev. Lett. **74**, 1446 (1995).

[36] D.S. Dessau, Z.-X. Shen, D.M. King, D. Marshall, L.W. Lombardo, P.H. Dickinson, A.G. Loeser, J. DiCarlo, C.-H. Park, A. Kapitulnik, and W.E. Spicer, Phys. Rev. Lett. **71**, 2781 (1993).

[37] M.C. Schabel, Z.-X. Shen, J.L. Peng, and R.L. Greene (unpublished).

[38] P.W. Anderson, Science **256**, 1526 (1992).

[39] R.B. Laughlin (private communication).

[40] Z.-X. Shen, R. S. List, D. S. Dessau, B. O. Wells, O. Jepsen, A. J. Arko, R. Barttlet, C. K. Shih, F. Parmigiani, J. C. Huang, and P. A. P. Lindberg, Phys. Rev. B **44**, 3604 (1991).